J Adv Ceram

Research Article

Texture development and surface reconstruction of $BiVO_4$ photoanode via one-pot hydrothermal reaction for enhanced photoelectrochemical water splitting

Sung Won Hwang[1,2,†], Yoo Jae Jeong[2,5,†], Runfa Tan[1,2], Indhujasri Saravanan[1,2], Hyun Soo Han[3], Dong Hoe Kim[4,✉], In Sun Cho[1,2,✉]

Cite this article: Hwang S, Jeong Y, Tan R, et al. *J Adv Ceram* 2025, **14**(3): 9221043. https://doi.org/10.26599/JAC.2025.9221043

ABSTRACT: The simultaneous optimization of the bulk and surface characteristics of photoelectrodes is essential to maximize their photoelectrochemical (PEC) performance. We report a novel one-pot hydrothermal synthesis of textured and surface-reconstructed $BiVO_4$ photoanodes (ts-BVO), achieving significant improvements in PEC water splitting. By controlling precursor molarity and ethylene glycol (EG) addition, we developed a stepwise dual reaction (SDR) mechanism, which enables simultaneous bulk texture development and surface reconstruction. The optimized CoBi/ts-BVO photoanode exhibited a photocurrent density of 4.3 mA·cm^{-2} at 1.23 V vs. reversible hydrogen electrode (RHE) with a high Faradaic efficiency of 98% under one sun illumination. Compared with nontextured $BiVO_4$, the charge transport efficiency increased from 8% to 70%, whereas the surface charge transfer efficiency improved from 9% to 85%. These results underscore the critical role of both bulk and surface engineering in enhancing PEC performance. Our findings offer a streamlined approach for improving the intrinsic properties of photoanodes in solar water splitting.

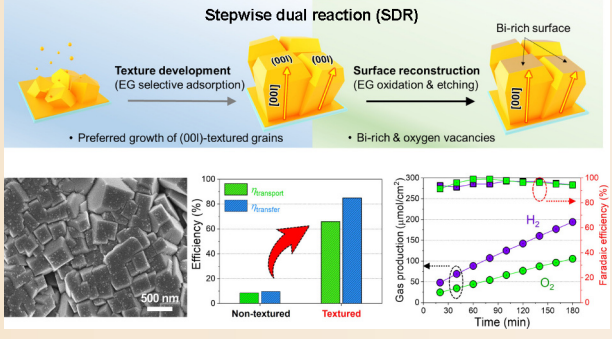

KEYWORDS: $BiVO_4$; hydrothermal; texture; surface reconstruction; ethylene glycol (EG); photoelectrochemical water splitting

1 Introduction

Bismuth vanadate ($BiVO_4$) has attracted considerable attention for its potential applications in photoelectrochemical (PEC) and photocatalytic (PC) oxidation reactions, which are crucial for producing clean hydrogen fuel from solar energy [1,2]. Owing to its narrow bandgap of 2.4 eV, $BiVO_4$ can absorb sunlight up to 520 nm, making it an attractive candidate for solar energy conversion. Additionally, it has an appropriate valence band edge for water oxidation, reasonable PEC and PC activities, and moderate physicochemical stability in neutral electrolytes [3–5]. However, several intrinsic limitations significantly hinder its performance, including low charge mobility, high bulk recombination rates, and sluggish oxygen evolution reaction (OER) kinetics at the surface [6]. Addressing these issues is essential for realizing the full potential of $BiVO_4$ as a photoanode material for water splitting.

Various strategies have been employed to improve the PEC performance of $BiVO_4$, among which texture engineering has emerged as a promising approach. By controlling the crystallographic orientation and exposed facets, texture engineering can enhance charge transport and reduce surface recombination, thereby improving the PEC efficiency. For example, $BiVO_4$ with preferential orientation along the [001] axis has demonstrated significant improvements in charge transport and photocurrent density [7–10]. Our previous work showed that the laser ablation method could be used to synthesize [001]-oriented $BiVO_4$, which resulted in a 71% charge transport efficiency and a photocurrent density of 3.9 mA·cm^{-2} at 1.23 V vs. the reversible hydrogen electrode (RHE) [11]. Similarly, Mo doping has been shown to enhance charge separation through texture development, further improving PEC performance [12,13]. However, these approaches typically focus on enhancing

† Sung Won Hwang and Yoo Jae Jeong contributed equally to this work.

[1] Department of Energy Systems Research, Ajou University, Suwon 16499, Republic of Korea. [2] Department of Material Science & Engineering, Ajou University, Suwon 16499, Republic of Korea. [3] Department of Mechanical Engineering, Stanford University, Stanford 94305, USA. [4] Department of Material Science & Engineering, Korea University, Seoul 02841, Republic of Korea. [5] Materials Science and Engineering Program, University of Colorado Boulder, Boulder 80303, USA.

✉ Corresponding authors. E-mail: D. Kim, donghoekim@korea.ac.kr; I. Cho, insuncho@ajou.ac.kr

Received: October 29, 2024; Revised: January 4, 2025; Accepted: February 6, 2025

bulk properties, often neglecting the surface-related factors that are equally crucial for PEC reactions.

Recent studies have revealed that the surface properties of $BiVO_4$, including surface stoichiometry and defect states, play a critical role in determining its PEC performance [14–18]. Defects related to vanadium, bismuth, and oxygen can significantly impact charge transport, carrier density, and surface reactivity, all of which are crucial for efficient water oxidation. In particular, surface recombination and poor oxygen evolution kinetics remain significant challenges, even in textured $BiVO_4$ [19–24]. Thus, while texture engineering improves bulk charge transport, it is often insufficient for maximizing overall PEC performance without simultaneous surface optimization.

To address these challenges, surface engineering techniques such as surface passivation and defect engineering have been applied to $BiVO_4$ [16,18]. These strategies aim to reduce surface recombination and improve the OER kinetics [25]. Surface modifications, such as incorporating protective layers or creating oxygen vacancies, have been shown to enhance surface charge transfer efficiency, but they often require additional processing steps, making the fabrication process more complex and time-consuming. Moreover, the independent optimization of bulk and surface properties can lead to inconsistencies in performance, as these two aspects are closely interconnected.

In this study, we propose a novel approach that simultaneously addresses both the bulk and surface limitations of $BiVO_4$ through a one-pot hydrothermal synthesis method. This approach enables the simultaneous optimization of texture development and surface reconstruction, utilizing a stepwise dual reaction (SDR) mechanism. By carefully controlling the molarity of the precursors and the concentration of ethylene glycol (EG), we achieve precise control over both bulk crystal growth and surface stoichiometry. EG plays a critical role in this process by facilitating [00l]-oriented growth in the early stages and inducing surface reconstruction during the later synthesis stages. This unified approach significantly enhances both the bulk charge transport efficiency and surface charge transfer efficiency, addressing the limitations of previous methods that focused on one aspect at a time.

The resulting textured and surface-reconstructed $BiVO_4$ (ts-BVO) photoanode with the CoBi electrocatalyst achieves a photocurrent density of 4.3 $mA{\cdot}cm^{-2}$ at 1.23 V vs. RHE, with a Faradaic efficiency of 98%, representing a substantial improvement over nontextured and nonreconstructed $BiVO_4$. This study highlights the importance of integrated bulk and surface engineering in the development of high-performance PEC photoanodes for solar water splitting, providing a streamlined, efficient method for enhancing the intrinsic properties of $BiVO_4$.

2 Experimental

2.1 Deposition of BVO seed layer

Prior to hydrothermal growth, a BVO nanoparticle film serving as a seed layer was deposited onto fluorine-doped tin oxide (FTO) glass substrates (Pilkington, TEC-8) via spin-coating. For this process, a 0.1 M BVO coating solution was prepared by dissolving bismuth nitrate pentahydrate ($Bi(NO_3)_3{\cdot}5H_2O$, 0.485 g, ≥ 98%, Sigma–Aldrich) and vanadyl acetylacetonate ($C_{10}H_4O_5V$, 0.265 g, 98%, Sigma–Aldrich) in a solvent mixture of 2-methoxyethanol ($C_3H_8O_2$, 6 mL, ≥ 99.3%, Alfa Aesar), acetic acid (CH_3COOH, 2 mL, 99%, Duksan) and 2,4-pentanedione ($C_5H_8O_2$, 2 mL, 99%, Alfa Aesar). The solution was ultrasonicated for 1 h and then aged at 25 °C for 12 h. Next, the coating solution was spin-coated onto the precleaned FTO substrates at 3000 r/min for 60 s. Intermediate annealing was performed at 300 °C for 10 min, followed by final annealing at 500 °C for 1 h in a box furnace.

2.2 Hydrothermal growth of ts-BVO

For hydrothermal growth, $Bi(NO_3)_3{\cdot}5H_2O$ (1.94 g, ≥ 98%, Sigma–Aldrich) and ammonium metavanadate (NH_4VO_3, 0.464 g, 99%, Sigma–Aldrich) were separately dissolved in EG ($C_2H_6O_2$, 25 mL, 99.8%, Sigma–Aldrich) and deionized water (25 mL) under stirring for 30 min at 80 °C to form solutions A and B, respectively. The solution B was subsequently added slowly to the solution A, and the mixture was stirred for 30 min until the temperature decreased to 25 °C. The resulting orange suspension (50 mL) was transferred to a Teflon-lined stainless-steel autoclave (100 mL), where the BVO seed layer-coated substrates were placed vertically. The autoclave was then sealed and maintained at 200 °C for 0.5–11 h. After the reaction, the samples were removed, rinsed with deionized water and ethanol, and dried under a nitrogen atmosphere. For electrochemical etching (to remove surface residues), chronoamperometry was conducted via a three-electrode cell with a Ag/AgCl reference electrode (3 M KCl), a BVO working electrode, and a platinum wire counter electrode. A constant external bias of 1.0 V vs. RHE was applied to the BVO sample for 30 s to remove surface residues. Finally, the BVO electrode was rinsed with deionized water and dried with flowing nitrogen.

2.3 Hydrothermal growth of textured (t-BVO) and nontextured BVO (n-BVO)

The same hydrothermal growth process was used to synthesize t-BVO and n-BVO, except for the precursor molarity and growth time. For t-BVO (textured without surface reconstruction), the precursor molarity was 0.08 M, and hydrothermal growth was conducted at 200 °C for 5 h. For n-BVO (nontextured and nonreconstructed), the precursor molarity was 0.06 M, and hydrothermal growth was conducted at 200 °C for 5 h.

3 Results and discussion

3.1 One-pot hydrothermal synthesis of ts-BVO

Figure 1(a) illustrates the one-pot hydrothermal synthesis of the ts-BVO photoanode, which followed an SDR mechanism utilizing EG. Before hydrothermal growth, a BVO nanoparticle seed layer was deposited on the FTO substrates via solution spin coating (Fig. S1 in the Electronic supplementary Material (ESM)). The seed layer-coated substrates were then subjected to hydrothermal treatment under controlled conditions, including variations in the precursor molarity, EG-to-water volume ratio, and growth time (Fig. S2 in the ESM). Texture development and surface reconstruction were achieved by adjusting the precursor molarity and the EG-to-water volume ratio.

EG plays a crucial role as the reaction medium owing to its unique physical and chemical properties [26]. During the early synthesis stages, EG was selectively adsorbed onto specific facets of the BVO nuclei, promoting oriented (textured) growth along the [00l] direction. Subsequently, EG undergoes self-oxidation, releasing electrons that selectively reduce the exposed (001) facets. This reduction led to the formation of a Bi-rich nonstoichiometric surface by etching. These two processes, texture development and surface reconstruction, occur sequentially and are facilitated by the SDR mechanism during one-pot hydrothermal synthesis, leading to the creation of highly textured and surface-reconstructed BVO photoanodes (referred to as ts-BVO).

An SEM image of the synthesized ts-BVO (Fig. 1(b)) reveals

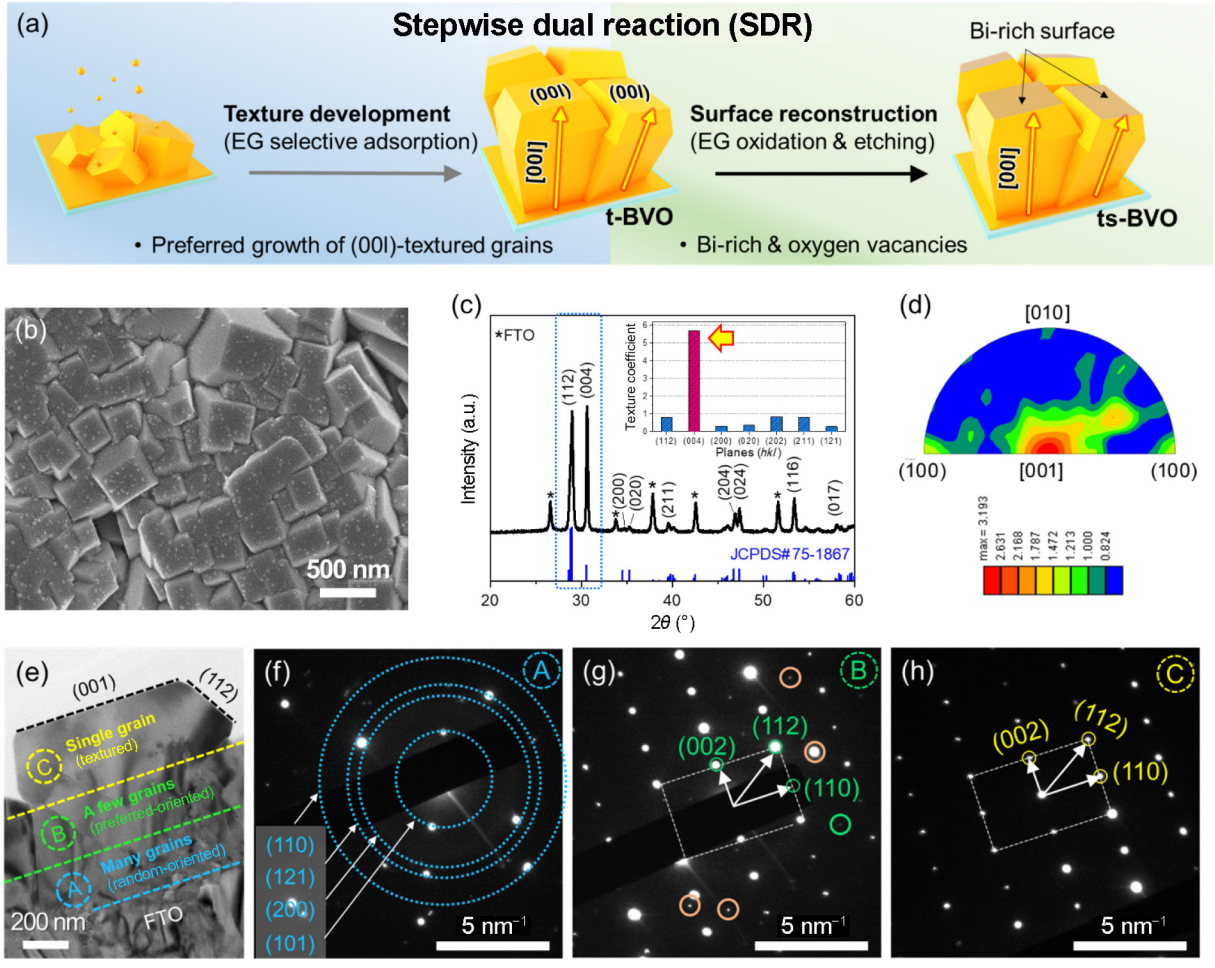

Fig. 1 One-pot hydrothermal synthesis of (00l)-textured and surface-reconstructed $BiVO_4$ (ts-BVO). (a) Schematic of stepwise dual-reaction synthesis. (b) Top-view scanning electron microscopy (SEM) image. (c) X-ray diffraction (XRD) pattern where the inset shows texture coefficient of selected planes. (d) Inverse pole figure. (e) Cross-sectional transmission electron microscopy (TEM) image and (f–h) corresponding selective area electron diffraction (SAED) patterns at the three different spots.

elongated decahedron-shaped grains with a high packing density. XRD analysis (Fig. 1(c)) confirmed the successful synthesis of monoclinic BVO (JCPDS No. 75-1867). Furthermore, the texture coefficient and inverse pole figure map (insets of Figs. 1(c) and 1(d)) demonstrate the dominance of the (00l) out-of-plane texture in ts-BVO. As shown in Fig. S3 in the ESM, ts-BVO was also successfully grown on quartz (an amorphous substrate), indicating that texture development was driven by kinetic factors rather than by epitaxial relationships with the underlying FTO substrate.

Transmission electron microscopy (TEM) revealed a decahedral morphology with smooth surfaces, exposing the (001) and (112) facets (Fig. 1(e)). Three distinct regions, denoted as 'A', 'B', and 'C', were examined. As shown in Fig. S4 in the ESM, the high-resolution TEM images revealed a monoclinic BVO phase in all three regions. Selective area electron diffraction (SAED) patterns indicate that region 'A' (at the bottom) consists of polycrystalline, randomly oriented small grains (Fig. 1(f)), whereas the region 'B' (in the middle) contains larger crystalline grains with a slight orientation (Fig. 1(g)). The region 'C' (at the top) comprises a large single-crystal grain (~600 nm in size), as evidenced by the SAED pattern (Fig. 1(h)). This gradient in the microstructure suggests that texture development occurred progressively during hydrothermal synthesis.

3.2 Critical parameters for texture development

To identify the critical factors for the textured growth of ts-BVO, we investigated the impact of precursor molarity on the growth rate, morphology, and texture coefficient (Figs. S5 and S6 in the ESM). As summarized in Fig. 2(a), the growth rate increased linearly with increasing precursor molarity but was moderate at molarities greater than 0.08 M, forming two distinct linear curves. This indicated a shift in the growth mechanism at molarities above 0.08 M. Figure 2(b) shows the variation in the texture coefficient for several crystal planes as a function of the precursor molarity. At a low molarity, the texture coefficients of the four planes were close to 1 (no texture development). However, at higher molarities (> 0.08 M), the texture coefficient of the (004) plane increases sharply, as confirmed by the intensified (004) XRD peaks (Fig. S6 in the ESM). This suggests that a precursor molarity greater than 0.08 M is critical for achieving strong (00l) texturing in ts-BVO.

Next, we explored the effect of the EG-to-water volume ratio on texture development during hydrothermal growth (Fig. 2(c), Fig. S7 in the ESM). At low EG-to-water volume ratios (0% and 20%), BVO exhibited rectangular plate-like grains aligned vertically on the FTO substrate, with a higher texture coefficient for the (200) plane than for the (00l) plane, indicating moderate (h00) texturing. However, at an EG-to-water volume ratio of 50%, decahedron-shaped grains with well-defined facets formed, indicating strong (00l) texturing. At 80%, the grains became rough and damaged, with nanorod-like shapes and reduced thicknesses. XRD and SEM analyses (Fig. S8 in the ESM) revealed the presence

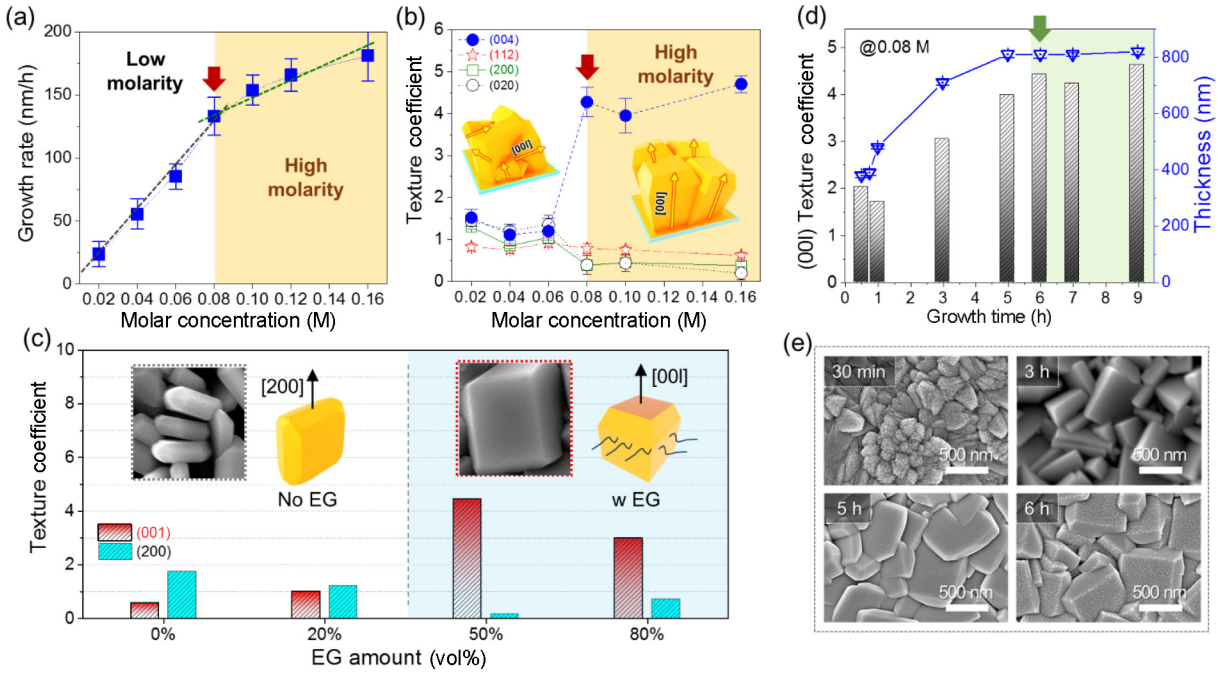

Fig. 2 Critical parameters for texture development of ts-BVO. (a) Effect of precursor molarity on growth rate. (b) Effect of precursor molarity on texture coefficient. (c) (001) texture coefficient variation with ethylene glycol (EG)-to-water mole ratio. (d) Texture coefficient variation with growth time. (e) Top-view SEM images at specific growth times.

of Bi metal peaks and a damaged surface, suggesting that EG played a key role in the chemical (reduction) reactions during hydrothermal growth [27,28]. Notably, even the damaged BVO grown at an EG-to-water volume ratio of 80% maintained a relatively high (00l) texture coefficient (Fig. 2(c)). According to Zhao *et al.* [29], EG can be adsorbed onto specific BVO crystal planes, promoting preferentially oriented growth. In addition, Chen *et al.* [30] reported that the EG-to-water volume ratio significantly influences the crystal growth of BVO, particularly by promoting orientation along the {004} facets. In this study, EG molecules were attached to the sidewalls of the BVO grains ({101}), facilitating [00l] textured growth.

The effects of growth time on the texture coefficient and film thickness were studied at 0.08 M (Fig. 2(d), Fig. S9 in the ESM). The (00l) texture coefficient increased with growth time, reached a maximum at the growth time of 5 h, and remained high up to 9 h. The film thickness followed a similar trend, suggesting that texture development was closely related to the film thickness. Cross-sectional TEM images further confirmed that the growth kinetics drive the (00l) texture development in ts-BVO (Fig. S10 in the ESM). Interestingly, after 5–9 h of growth, there was no significant increase in the film thickness or growth rate (Figs. S11 and S12 in the ESM). Furthermore, the postsynthesis solution pH demonstrated a trend analogous to that of the growth rate. Under controlled synthesis conditions (0.08 M, 200 °C, and 6 h), the temporal evolution of pH was investigated (Fig. S13 in the ESM). The results revealed a rapid increase in pH during the initial 3 h, subsequently reaching a plateau. This inflection point coincided with the onset of a gradual decline in growth rate. To rigorously assess the effect of pH on crystal growth, BVO was synthesized under low and high initial pH conditions (0.4 and 4.2, respectively) while all other parameters were held constant. Notably, after 6 h of synthesis, the low-pH BVO resulted in significantly greater film growth, exceeding approximately 3 μm, than did the high-pH BVO, which resulted in a substantially reduced film thickness of less than ~80 nm. These findings underscore the critical role of the solution pH in influencing the crystal growth process.

Top-view SEM images captured at various growth stages (30 min, 3 h, 5 h, and 6 h) revealed the progressive evolution of the surface morphology (Fig. 2(e)). At 30 min, the BVO exhibited randomly oriented grains with small nanoparticles, resembling a bumpy "crocodile skin" appearance, suggesting that an oriented attachment mechanism governed growth [31,32]. As the growth time increased to 5 h, the grains transitioned to smooth decahedral shapes with larger grain sizes (~600 nm). However, after 6 h of growth, the grains became thicker, and nanoparticles formed exclusively on the (001) facet, indicating surface reconstruction. These nanoparticles continued to grow as the reaction progressed (Fig. S11 in the ESM). Previous studies have shown that the (001) and (101) facets of BVO correspond to the reduction and oxidation facets, respectively [33,34]. Therefore, the (001) surface was preferentially reduced during prolonged hydrothermal growth. At 11 h, XRD analysis (Fig. S14 in the ESM) revealed the formation of VO_x flakes and Bi metal, along with a diminished (004) peak intensity, indicating excessive reduction and surface reconstruction in the later stages of hydrothermal growth. At 18 h, EDS mapping revealed that these spheres are primarily rich in Bi, with less V, indicating an enrichment of metallic Bi (Fig. S15 in the ESM). These SEM and EDS results align well with the XRD analysis, confirming that the reduction reaction facilitated by EG.

For comparison, BVO was further synthesized at a low precursor molarity (0.06 M) by varying the growth time. Notably, no specific texture development was observed, even at prolonged growth times (> 6 h). However, surface chemical reactions, including nanoparticle formation, were still observed with prolonged growth (Fig. S16 in the ESM). This suggests that the chemical reaction occurs regardless of the precursor molarity, but texture development requires a higher molarity.

3.3 Surface reconstruction mechanism

Electrochemical etching was used to remove the surface-formed nanoparticles in the 6 h ts-BVO sample. After electrochemical etching, the SEM images revealed a smooth surface with no

residue (Fig. S17 in the ESM). The electrochemical etching voltage was controlled to determine its impact on the surface morphology and PEC performance (Fig. S18 in the ESM). The etching voltage had a minimal impact on the PEC performance, indicating that surface reconstruction is primarily attributed to the addition of EG. Notably, BVO demonstrates good chemical stability at approximately pH 9 and within an etching voltage range of 0–1.0 V. However, vanadium species readily dissolve into ionic forms under these conditions [35]. Well-known NaOH-based chemical etching is challenging due to the uneven morphology of BVO, which can lead to nonuniform etching across the surface. An uneven surface morphology and a decrease in the photocurrent density were observed with increasing NaOH etching duration (30 min), which was attributed to overetching (Fig. S19 in the ESM). To address the limitations of the NaOH-based etching method, we utilized electrochemical etching, which ensures uniform surface modification by leveraging the electrochemical stability window, resulting in a more uniform and stable BVO photoanode. XPS analysis of the three samples (5 h, 6 h, and 6 h/etched) revealed changes in the surface composition (Fig. 3(a), Fig. S20 in the ESM). The Bi : V stoichiometry remained at approximately 1 : 1 (52% Bi) for the 5 h sample. However, the Bi content of the 6 h sample sharply decreased (8% Bi), indicating a V-rich surface. Similar to the 11 h sample (Fig. S14 in the ESM), this 8% Bi content indicated the formation of VO_x due to the surface reduction effect. Notably, after etching (removing the surface nanoparticles), the Bi content again increased to 62%, suggesting the formation of a Bi-rich surface. In addition, this 6-h/etched sample exhibited many oxygen vacancies and a high V^{4+} content at the surface. Raman analysis confirmed that surface reconstruction had little effect on the crystalline structure (Fig. S21 in the ESM). EG, known as a reducing agent, facilitates surface reconstruction by reducing Bi–O bonds, which are weaker than V–O bonds in the BVO structure [14,36]. This led to preferential Bi–O bond cleavage and the formation of a VO_x layer during prolonged hydrothermal growth (Fig. S14 in the ESM). After electrochemical etching, the surface reverts to a Bi-rich state. This Bi-rich surface plays a key role in surface reaction kinetics and band-edge modulation, enhancing the PEC performance [37,38].

Figure 3(b) shows the reaction pathway for EG decomposition (self-oxidation) during the hydrothermal process. According to previous studies, EG undergoes self-oxidation in the presence of water and BVO precursor ions, producing byproducts and electrons [39,40]. EG is oxidized to glycolaldehyde, which is then cleaved into formate via C–C bond oxidation. Formate, a stable product, participates in the chemical reduction of the BVO surface, leading to surface reconstruction. To verify the self-oxidation of EG, ^{1}H NMR analysis was performed on the remaining hydrothermal solutions. On the basis of theoretical calculations, the peak between 4 and 4.5 ppm was identified as glycolic acid, and the peak between 8 and 8.5 ppm was attributed to formic acid (Fig. S22 in the ESM). The predominant peaks of glycolic and formic acids were clearly observed in the solution after 6 h of growth (Figs. 3(c) and 3(d)), confirming that EG self-oxidation occurred. The leftward peak shift at 3 h is attributed to changes in the pH of the hydrothermal solution [41]. Generally, the color of a vanadium-containing solution varies depending on the oxidation state of the vanadium [42,43]. At 0 h, the solution appeared yellow (indicating the +5 oxidation state). As the reaction progressed, the color of the solution gradually changed to green or light blue, suggesting a reduction in the oxidation state of vanadium from +5 to +4 or +3. Thus, the formation of formic acid and the color change of the solution highlight the crucial role of EG as a reducing agent in the surface reconstruction process.

The synthesis temperature was varied to investigate the decomposition behavior of EG and the reaction kinetics. Figure S23 in the ESM shows that the (001) texture coefficient increases as the temperature increases, whereas the thickness remains constant between 160 and 200 °C. Surface reconstruction, identified by surface particles, occurs exclusively at 200 °C. Rapid BVO growth occurs above 160 °C due to the high concentration of the precursor solution, but EG decomposition is achieved only

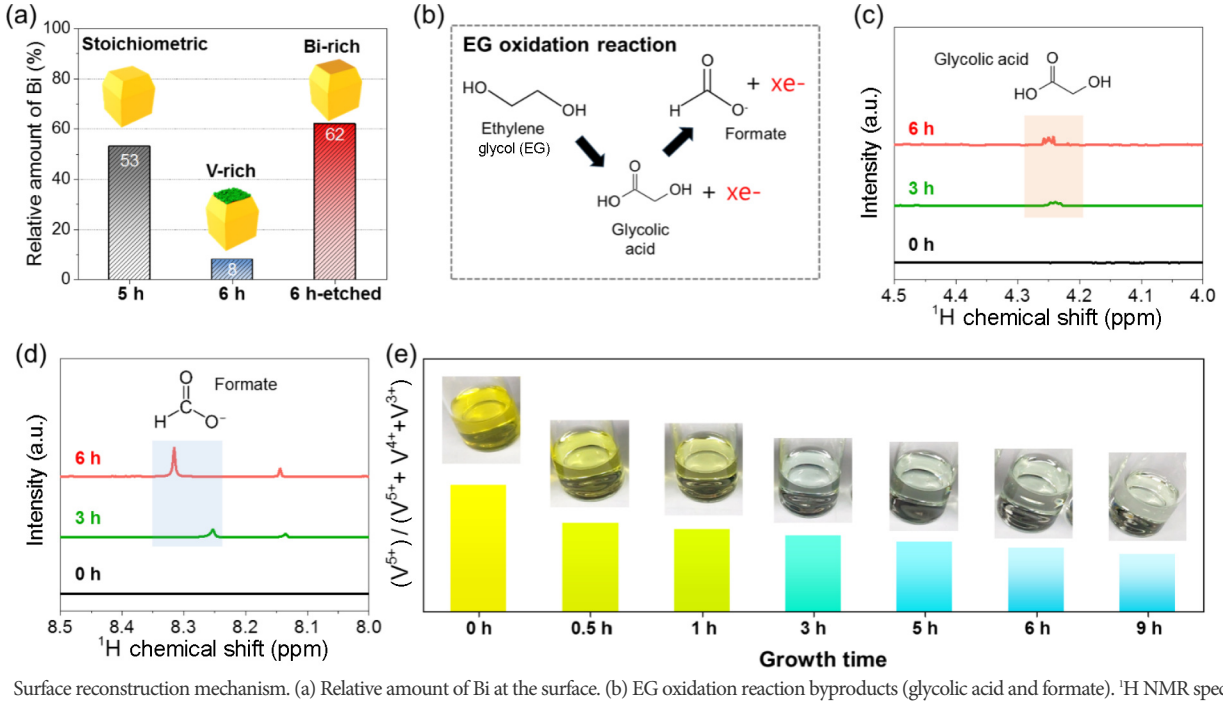

Fig. 3 Surface reconstruction mechanism. (a) Relative amount of Bi at the surface. (b) EG oxidation reaction byproducts (glycolic acid and formate). ^{1}H NMR spectra of hydrothermal growth solution after specific reaction times: (c) glycolic acid and (d) formate. (e) The color of solution changed with increasing hydrothermal reaction time: yellow: V^{5+}, blue: V^{4+}, and green: V^{3+}.

清華大学出版社 Tsinghua University Press | SciOpen

at 200 °C, given its boiling point of 197 °C. Consequently, texture development and surface reconstruction are achieved only at temperatures above 200 °C.

Figure S24 in the ESM depicts the proposed hydrothermal growth mechanism via SDR. The introduction of EG into the growth solution serves a dual purpose: EG acts as a capping and reducing agent, facilitating anisotropic growth through preferential adsorption at specific facets and enabling a surface reduction reaction. During the initial stage, BVO rapidly nucleates on the seed layer with random orientations. Over time, texture development occurred, forming smooth grains with preferentially oriented facets within 5 h of growth. However, in the later stages, as precursor consumption is completed, EG acts as a reducing agent, initiating surface reconstruction. Consequently, the surface of the BVO photoanode is transformed into a Bi-rich surface *in situ*. Finally, as shown in Fig. S25 in the ESM, the optimized synthesis conditions were as follows: precursor molarity of 0.08 M; growth temperature of 200 °C, growth time of 6 h, and EG-to-water volume ratio of 50%.

3.4 Photoelectrochemical (PEC) performance and Faradaic efficiency

The PEC performances of the ts-BVO photoanodes were measured in a 1 M borate buffer (KBi, pH 9.4) electrolyte via a three-electrode setup (Fig. 4(a)). For comparison, nontextured (n-BVO) and textured BVO (t-BVO, without surface reconstruction) photoanodes with the same thickness (~800 nm) were also evaluated (Fig. S26 in the ESM). Figure 4(b) shows the photocurrent density versus potential (*J*–*V*) curves of the three BVO photoanodes. The photocurrent density at 1.23 V vs. RHE ($J_{ph,\ 1.23\ V}$) of ts-BVO, t-BVO and n-BVO was measured to be 3.2, 1.0, and 0.2 mA·cm^{-2}, respectively (Fig. 4(b)). ts-BVO achieved a $J_{ph\ 1.23\ V}$ that which was approximately 3 times greater than that of t-BVO and 16 times greater than that of the n-BVO photoanode. The maximum applied bias photon-to-current efficiency (ABPE) of ts-BVO was 0.55%, which is approximately three times greater than that of t-BVO (0.17%) and 28 times greater than that of n-BVO (0.02%) (Fig. S27 in the ESM). Compared with t-BVO and n-BVO, ts-BVO presented significantly greater values across the wavelength range of 300–510 nm (Fig. 4(c)). Furthermore, the integrated IPCE values of ts-BVO, t-BVO, and n-BVO are 2.9, 0.7, and 0.2 mA·cm^{-2}, respectively, which are consistent with the *J*–*V* curves. As shown in Table S1 in the ESM, the photocurrent density of ts-BVO was compared to that of BVO photoanodes synthesized via diverse methods reported in recent years. Notably, ts-BVO has one of the highest photocurrent densities among reported BVO photoanodes, highlighting the effectiveness of texture development and surface reconstruction strategies. These results suggest that the enhanced PEC performance of ts-BVO arises from the combined effects of its bulk and surface characteristics, which are optimized through texturing and surface reconstruction.

To investigate the key factors contributing to the enhanced photocurrent, electrochemical impedance spectroscopy (EIS) was

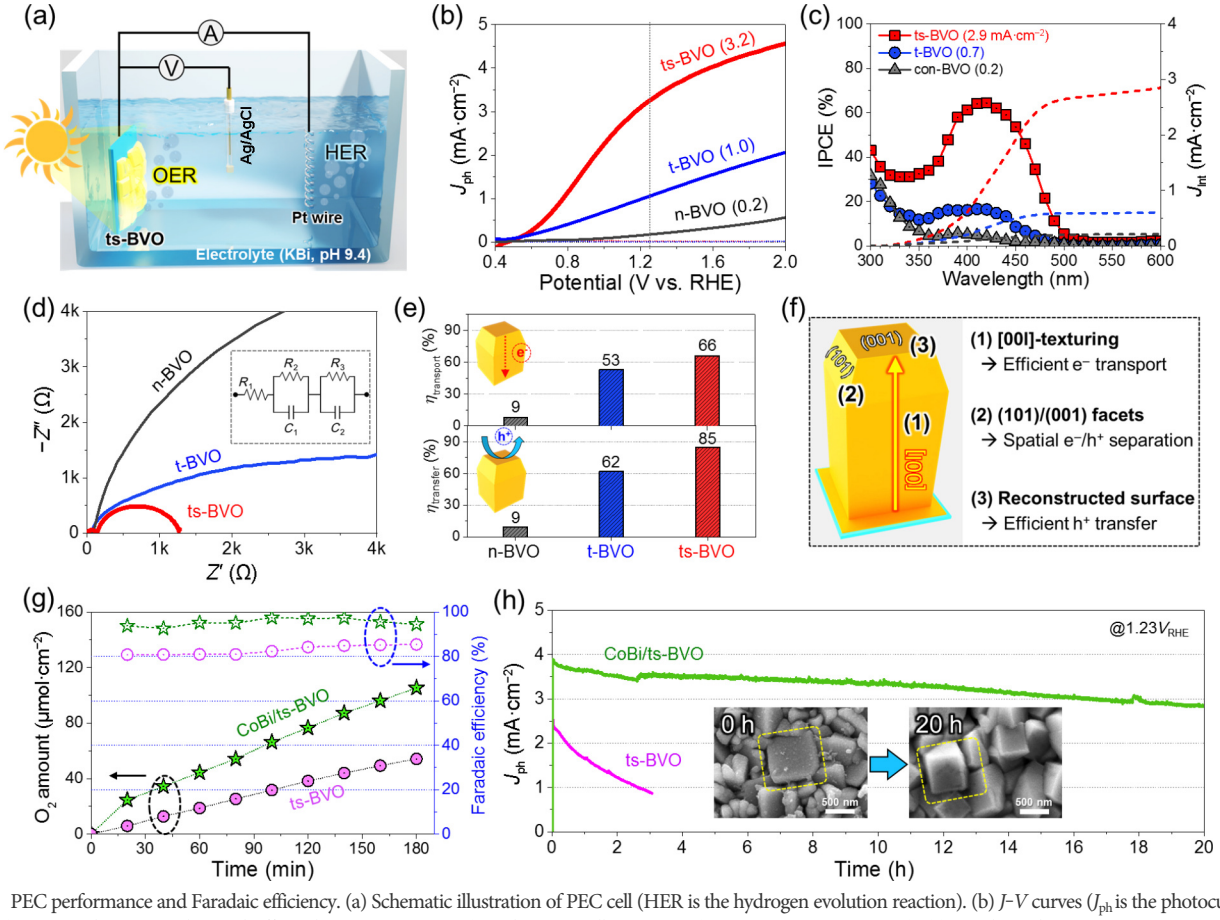

Fig. 4 PEC performance and Faradaic efficiency. (a) Schematic illustration of PEC cell (HER is the hydrogen evolution reaction). (b) *J*-*V* curves (J_{ph} is the photocurrent density) measured in a 1 M borate buffer solution (KBi, pH 9.4) under 1 sun illumination (AM 1.5 G, 100 mW·cm^{-2}). (c) Incident photon-to-current conversion efficiency (IPCE). (d) Electrochemical impedance spectroscopy (EIS) analysis. The inset is an equivalent circuit model used for fitting. (e) Comparison of the charge transport ($\eta_{transport}$) and charge transfer ($\eta_{transfert}$) efficiencies at 1.23 V vs. RHE. (f) Summary of the advantages of ts-BVO for PEC water oxidation. (g) Gas evolution and Faradaic efficiency of ts-BVO and CoBi OEC deposited ts-BVO (CoBi/ts-BVO). (h) Photocurrent stability of ts-BVO and CoBi/ts-BVO measured at 1.23 V vs. RHE.

performed (Fig. 4(d)). The extracted values of the series resistance (R_1), bulk resistance (R_2), and interfacial charge-transfer resistance (R_3) are listed in Table S2 in the ESM. Notably, ts-BVO exhibited the smallest semicircle, indicating significant improvements in both the bulk charge transport and surface charge transfer properties. Next, the charge transport ($\eta_{transport}$) and transfer efficiencies ($\eta_{transfer}$) of three BVO photoanodes were quantified at 1.23 V vs. RHE via a hole scavenger method (Fig. 4(e), Figs. S28 and S29 in the ESM) [44,45]. The results revealed that, compared with n-BVO (9%), ts-BVO and t-BVO achieved significantly greater $\eta_{transport}$ (> 53%), indicating that (00l)-texturing strongly enhances charge transport. Previous studies have demonstrated that specific crystal facets, such as (001) and (101), and texturing contribute to enhanced photocurrent density owing to spatial charge separation and efficient transport characteristics [11,46,47]. Theoretical calculations also support this finding, showing that electron transfer along the [001] direction has the lowest activation energy [47]. Our results also highlight the advantages of (00l)-textured BVO for efficient electron transport along the [00l] direction. Additionally, compared with t-BVO (62%), ts-BVO exhibited greatly improved $\eta_{transfer}$ (85%), which was attributed to the Bi-rich surface resulting from surface reconstruction.

The optical properties (absorption, reflectance, and transmittance spectra) and photographs of the three BVO photoanodes were also examined (Fig. S30 in the ESM). Although ts-BVO exhibited slightly greater light absorption (~86%), the light absorption properties of all three BVO photoanodes were generally comparable. This suggests that (00l)-texturing and surface reconstruction have little impact on the optical properties. The advantages of ts-BVO for enhancing PEC performance are summarized in Fig. 4(f). The combination of (00l) texturing improved the charge separation and transport efficiencies for both electrons and holes. Furthermore, the reconstructed surface (Bi-rich) enables more efficient hole transfer during the OER. To examine the effect of EG on surface modification (reduction), TiO_2 and Fe_2O_3 photoanodes [48–50] were hydrothermally treated with EG (Fig. S31 in the ESM). These results indicate that, compared with their pristine counterparts, EG-treated photoanodes exhibit greatly improved photocurrent densities. A darker surface was also observed on the EG-treated photoanode samples, suggesting surface composition or property alterations. These findings emphasize the critical role of EG in enhancing surface modification/reconstruction and PEC performance.

Finally, the oxygen gas evolution rates and Faradaic efficiencies (FEs) of the three BVO photoanodes were evaluated via gas chromatography (GC) measurements during 3 h of PEC operation (Fig. S32 in the ESM). Notably, the oxygen gas evolution rate was approximately 19 $\mu mol \cdot cm^{-2} \cdot h^{-1}$, which is approximately 5 times greater than that of t-BVO (~4 $\mu mol \cdot cm^{-2} \cdot h^{-1}$) and 180 times greater than that of n-BVO (0.1 $\mu mol \cdot cm^{-2} \cdot h^{-1}$). XPS analysis confirmed that the ts-BVO surface underwent an *in situ* transformation into a Bi-rich surface with abundant oxygen vacancies owing to EG oxidation.

Previous studies by Lee *et al.* [37] showed that Bi-rich surfaces exhibit more favorable surface energetics for PEC water oxidation, leading to a higher photocurrent density and oxygen evolution rate. Therefore, the superior PEC performance of ts-BVO is attributed to the synergistic effects of texture development and surface reconstruction (Fig. 4(f)).

The PEC performance of ts-BVO was further improved by depositing a CoBi electrocatalyst on its surface (Fig. S33 in the ESM). The energy dispersive spectroscopy (EDS) mapping results confirmed the homogeneous and uniform deposition of the CoBi electrocatalyst across the entire region (Fig. S34 in the ESM). Electrocatalysts play a crucial role in enhancing surface kinetics and mitigating photocorrosion, thereby improving the overall PEC performance of BVO [51]. As shown in Figs. S35 and S36 in the ESM, CoBi/ts-BVO has a greatly increased $J_{ph\,1.23\,V}$ of 4.3 $mA \cdot cm^{-2}$ and a cathodic shift of approximately 200 mV compared with that of ts-BVO (3.2 $mA \cdot cm^{-2}$), which is attributed to the superior water oxidation kinetics of CoBi [52,53]. Additionally, the oxygen evolution rate of CoBi/ts-BVO is 35 $\mu mol \cdot cm^{-2} \cdot h^{-1}$, which is twice that of ts-BVO (18 $\mu mol \cdot cm^{-2} \cdot h^{-1}$). More importantly, CoBi/ts-BVO achieved stable and nearly uniform FE (~98%) (Fig. 4(g)).

Finally, long-term photocurrent stability tests were conducted at 1.23 V vs. RHE (Fig. 4(h), Fig. S32 in the ESM). Notably, textured BVOs (both t-BVO and ts-BVO) maintained a smooth surface, whereas n-BVO presented tiny surface particles, likely resulting from photocorrosion (Fig. S37 in the ESM). Additionally, t-BVO exhibited a relatively stable photocurrent density compared with n-BVO, which was attributed to its well-developed (001) textured morphology (Fig. S32(a) in the ESM). However, a gradual decrease in the photocurrent density was observed in the *J–t* curve, which was attributed primarily to the dissolution of V^{5+} ions from the BVO surface during PEC operation [54]. Importantly, CoBi/ts-BVO retained 75% of its initial photocurrent, even after 20 h of continuous operation. After 20 h, SEM analysis revealed that the CoBi/ts-BVO layer had smoothed out, suggesting partial removal or dissolution of the CoBi layer. We believe that redeposition or regeneration strategies for electrocatalysts can enhance the long-term stability of ts-BVO photoanodes for practical applications.

4 Conclusions

We successfully developed a novel one-pot hydrothermal growth method based on an SDR mechanism to synthesize ts-BVO photoanodes. Our study demonstrated that key growth parameters, such as precursor molarity and the addition of EG, substantially impact growth kinetics, thereby influencing both texturing and surface reconstruction. EG was found to play a critical role in both the initial texture development stage and the later surface reconstruction stage. The optimized ts-BVO photoanode achieved a photocurrent density of 3.2 $mA \cdot cm^{-2}$ at 1.23 V vs. RHE, which was nearly 20 times greater than those of nontextured and nonsurface-reconstructed BVOs. This improvement in the photocurrent density is attributed to enhanced charge collection, facilitated by the formation of (00l)-textured and Bi-rich surfaces. Furthermore, when coupled with a CoBi oxygen evolution electrocatalyst, ts-BVO achieved an even higher photocurrent density of 4.3 $mA \cdot cm^{-2}$ at 1.23 V vs. RHE, along with an impressive Faradaic efficiency of 98%. These findings provide valuable insights for improving the intrinsic properties of photoanodes for more efficient solar water splitting.

Acknowledgements

This work was supported by the National Research Foundation of Korea (NRF) grant funded by the Korean government (MSIT) (No. RS-2024-00335976). This work was also supported by the Korea Institute of Energy Technology Evaluation Planning (KETEP) from the Ministry of Trade, Industry, Energy (No. 20214000000680).

Declaration of competing interest

The authors have no competing interests to declare that are relevant to the content of this article.

Electronic Supplementary Material

Supplementary material is available in the online version of this article at https://doi.org/10.26599/JAC.2024.9221043.

References

[1] Grätzel M. Photoelectrochemical cells. *Nature* 2001, **414**: 338–344.

[2] Walter MG, Warren EL, McKone JR, *et al.* Solar water splitting cells. *Chem Rev* 2010, **110**: 6446–6473.

[3] Wang G, Wang H, Ling Y, *et al.* Hydrogen-treated TiO_2 nanowire arrays for photoelectrochemical water splitting. *Nano Lett* 2011, **11**: 3026–3033.

[4] Sivula K, Le Formal F, Grätzel M. Solar water splitting: Progress using hematite (α-Fe_2O_3) photoelectrodes. *ChemSusChem* 2011, **4**: 432–449.

[5] Sivula K, Le Formal F, Grätzel M. WO_3–Fe_2O_3 photoanodes for water splitting: A host scaffold, guest absorber approach. *Chem Mater* 2009, **21**: 2862–2867.

[6] Park Y, McDonald KJ, Choi KS. Progress in bismuth vanadate photoanodes for use in solar water oxidation. *Chem Soc Rev* 2013, **42**: 2321–2337.

[7] Li D, Liu Y, Shi WW, *et al.* Crystallographic-orientation-dependent charge separation of $BiVO_4$ for solar water oxidation. *ACS Energy Lett* 2019, **4**: 825–831.

[8] Wang Z, Dong C, Liang S, *et al.* Preparation of textured and transparent $BiVO_4$ photoelectrodes based on Mo-doped $BiVO_4$ nanoparticles for constructing a stand-alone tandem water splitting device. *Chem Commun* 2020, **56**: 4156–4159.

[9] Yoon H, Mali MG, Choi JY, *et al.* Nanotextured pillars of electrosprayed bismuth vanadate for efficient photoelectrochemical water splitting. *Langmuir* 2015, **31**: 3727–3737.

[10] Zhang BY, Xiang Y, Guo M, *et al.* Fabrication of a facet-oriented $BiVO_4$ photoanode by particle engineering for promotion of charge separation efficiency. *ACS Appl Energy Mater* 2021, **4**: 4259–4268.

[11] Han HS, Shin S, Kim DH, *et al.* Boosting the solar water oxidation performance of a $BiVO_4$ photoanode by crystallographic orientation control. *Energy Environ Sci* 2018, **11**: 1299–1306.

[12] Ye KH, Li HB, Huang D, *et al.* Enhancing photoelectrochemical water splitting by combining work function tuning and heterojunction engineering. *Nat Commun* 2019, **10**: 3687.

[13] Nair V, Perkins CL, Lin QY, *et al.* Textured nanoporous Mo: $BiVO_4$ photoanodes with high charge transport and charge transfer quantum efficiencies for oxygen evolution. *Energy Environ Sci* 2016, **9**: 1412–1429.

[14] Lu Y, Yang YL, Fan XY, *et al.* Boosting charge transport in $BiVO_4$ photoanode for solar water oxidation. *Adv Mater* 2022, **34**: 2108178.

[15] Trześniewski BJ, Digdaya IA, Nagaki T, *et al.* Near-complete suppression of surface losses and total internal quantum efficiency in $BiVO_4$ photoanodes. *Energy Environ Sci* 2017, **10**: 1517–1529.

[16] Gao RT, Wang L. Stable cocatalyst-free $BiVO_4$ photoanodes with passivated surface states for photocorrosion inhibition. *Angew Chem Int Ed* 2020, **59**: 23094–23099.

[17] Wang SC, He TW, Chen P, *et al.* In situ formation of oxygen vacancies achieving near-complete charge separation in planar $BiVO_4$ photoanodes. *Adv Mater* 2020, **32**: 2001385.

[18] Wang H, Gao RT, Wang L. Boosting charge separation and transfer at the boron-triggered $BiVO_4$ interface for efficient and stable solar water splitting. *Chem Eng J* 2023, **465**: 142571.

[19] Kim JH, Lee JS. Elaborately modified $BiVO_4$ photoanodes for solar water splitting. *Adv Mater* 2019, **31**: 1806938.

[20] Liu X, Liu Y, Liu TF, *et al.* Alkali-mediated dissolution-recrystallization strategy for *in situ* construction of a $BiVO_4/Bi_{25}VO_{40}$ heterojunction with promoted interfacial charge transfer: Formation mechanism and photocatalytic tetracycline degradation studies. *Chem Eng J* 2022, **431**: 134181.

[21] Wang SC, Chen P, Bai Y, *et al.* New $BiVO_4$ dual photoanodes with enriched oxygen vacancies for efficient solar-driven water splitting. *Adv Mater* 2018, **30**: 1800486.

[22] Liu BY, Wang X, Zhang YJ, *et al.* A $BiVO_4$ photoanode with a VO_x layer bearing oxygen vacancies offers improved charge transfer and oxygen evolution kinetics in photoelectrochemical water splitting. *Angew Chem Int Ed* 2023, **62**: 202217346.

[23] Wang SC, Wang X, Liu BY, *et al.* Vacancy defect engineering of $BiVO_4$ photoanodes for photoelectrochemical water splitting. *Nanoscale* 2021, **13**: 17989–18009.

[24] Li C, Feng F, Jian J, *et al.* Boosting carrier dynamics of $BiVO_4$ photoanode via heterostructuring with ultrathin BiOI nanosheets for enhanced solar water splitting. *J Mater Sci Technol* 2021, **79**: 21–28.

[25] Tan RF, Sivanantham A, Jansi Rani B, *et al.* Recent advances in surface regulation and engineering strategies of photoelectrodes toward enhanced photoelectrochemical water splitting. *Coord Chem Rev* 2023, **494**: 215362.

[26] Hojamberdiev M, Zhu GQ, Kadirova ZC, *et al.* Morphology-controlled growth of $BiVO_4$ crystals by hydrothermal method assisted with ethylene glycol and ethylenediamine and their photocatalytic activity. *Mater Chem Phys* 2015, **165**: 188–195.

[27] Shit S, Jang W, Bolar S, *et al.* Effect of the solvent ratio (ethylene glycol/water) on the preparation of an iron sulfide electrocatalyst and its activity towards overall water splitting. *ChemElectroChem* 2019, **6**: 3199–3208.

[28] Wang QZ, He JJ, Shi YB, *et al.* Designing non-noble/semiconductor Bi/$BiVO_4$ photoelectrode for the enhanced photoelectrochemical performance. *Chem Eng J* 2017, **326**: 411–418.

[29] Zhao GS, Liu W, Hao Y, *et al.* Nanostructured shuriken-like $BiVO_4$ with preferentially exposed{010}facets: Preparation, formation mechanism, and enhanced photocatalytic performance. *Dalton Trans* 2018, **47**: 1325–1336.

[30] Chen L, Wang JX, Meng DW, *et al.* Enhanced photocatalytic activity of hierarchically structured $BiVO_4$ oriented along{040}facets with different morphologies. *Mater Lett* 2015, **147**: 1–3.

[31] Xue XG, Penn RL, Leite ER, *et al.* Crystal growth by oriented attachment: Kinetic models and control factors. *CrystEngComm* 2014, **16**: 1419–1429.

[32] Cao DD, Gong S, Shu XG, *et al.* Preparation of ZnO nanoparticles with high dispersibility based on oriented attachment (OA) process. *Nanoscale Res Lett* 2019, **14**: 210.

[33] Liu T, Pan ZH, Kato K, *et al.* A general interfacial-energetics-tuning strategy for enhanced artificial photosynthesis. *Nat Commun* 2022, **13**: 7783.

[34] Li D, Chen RT, Wang PP, *et al.* Effect of facet-selective assembly of cocatalyst on $BiVO_4$ photoanode for solar water oxidation. *Chem Cat Chem* 2019, **11**: 3763–3769.

[35] Jung G, Byun S, Shin B. Improving uniformity and reproducibility of photoelectrochemical water oxidation performance of $BiVO_4$ photoanodes via selective removal of excess V_2O_5 by electrochemical etching. *ACS Appl Energy Mater* 2020, **3**: 7756–7763.

[36] Li GL. First-principles investigation of the surface properties of fergusonite-type monoclinic $BiVO_4$ photocatalyst. *RSC Adv* 2017, **7**: 9130–9140.

[37] Lee D, Wang WN, Zhou CY, *et al.* The impact of surface composition on the interfacial energetics and photoelectrochemical properties of $BiVO_4$. *Nat Energy* 2021, **6**: 287–294.

[38] Chen XT, Zhen C, Li N, *et al.* Photochemically etching $BiVO_4$ to construct asymmetric heterojunction of $BiVO_4/BiO_x$ showing efficient photoelectrochemical water splitting. *Small Meth* 2023, **7**: 2201611.

[39] Ren TL, Yu Z, Yu HJ, *et al.* Sustainable ammonia electrosynthesis from nitrate wastewater coupled to electrocatalytic upcycling of polyethylene terephthalate plastic waste. *ACS Nano* 2023, **17**: 12422–12432.

[40] Zhang BW, Zhang HY, Pan YY, *et al.* Photoelectrochemical

conversion of plastic waste into high-value chemicals coupling hydrogen production. *Chem Eng J* 2023, **462**: 142247.

[41] Berregi I, del Campo G, Caracena R, *et al.* Quantitative determination of formic acid in apple juices by 1H NMR spectrometry. *Talanta* 2007, **72**: 1049–1053.

[42] Jeong YJ, Seo DH, Baek JH, *et al.* Crystal reconstruction of Mo: $BiVO_4$: Improved charge transport for efficient solar water splitting. *Adv Funct Mater* 2022, **32**: 2208196.

[43] Hu P, Hu P, Vu TD, *et al.* Vanadium oxide: Phase diagrams, structures, synthesis, and applications. *Chem Rev* 2023, **123**: 4353–4415.

[44] Qu L, Tan RF, Sivanantham A, *et al.* Point-defect engineering of nanoporous $CuBi_2O_4$ photocathode via rapid thermal processing for enhanced photoelectrochemical activity. *J Energy Chem* 2022, **71**: 201–209.

[45] Jeong YJ, Tan RF, Nam S, *et al.* Rapid surface reconstruction of In_2S_3 photoanode via flame treatment for enhanced photoelectrochemical performance. *Adv Mater* 2024: 2403164.

[46] Jeong YJ, Hwang SW, Chaikasetsin S, *et al.* Dual textured $BiVO_4$/Sb: SnO_2 heterostructure for enhanced photoelectrochemical water-splitting. *Chem Eng J* 2022, **435**: 135183.

[47] Liu TF, Zhou X, Dupuis M, *et al.* The nature of photogenerated charge separation among different crystal facets of $BiVO_4$ studied by density functional theory. *Phys Chem Chem Phys* 2015, **17**: 23503–23510.

[48] Cho IS, Logar M, Lee CH, *et al.* Rapid and controllable flame reduction of TiO_2 nanowires for enhanced solar water-splitting. *Nano Lett* 2014, **14**: 24–31.

[49] Kim JU, Han HS, Park J, *et al.* Facile and controllable surface-functionalization of TiO_2 nanotubes array for highly-efficient photoelectrochemical water-oxidation. *J Catal* 2018, **365**: 138–144.

[50] Cho IS, Han HS, Logar M, *et al.* Enhancing low-bias performance of hematite photoanodes for solar water splitting by simultaneous reduction of bulk, interface, and surface recombination pathways. *Adv Energy Mater* 2016, **6**: 1501840.

[51] McDowell MT, Lichterman MF, Spurgeon JM, *et al.* Improved stability of polycrystalline bismuth vanadate photoanodes by use of dual-layer thin TiO_2/Ni coatings. *J Phys Chem C* 2014, **118**: 19618–19624.

[52] Kumar S, Satpati AK. Investigation of interfacial charge transfer kinetics of photocharged Co–Bi modified $BiVO_4$ using scanning electrochemical microscopy (SECM). *Electrochim Acta* 2021, **368**: 137565.

[53] Dell'Oro R, Sansotera M, Bianchi CL, *et al.* Efficient $BiVO_4$-based photoanode with chemically precipitated hierarchical cobalt borate ($Co–B_i$) oxygen evolution reaction catalysts. *ACS Omega* 2023, **8**: 20332–20341.

[54] Lee DK, Choi KS. Enhancing long-term photostability of $BiVO_4$ photoanodes for solar water splitting by tuning electrolyte composition. *Nat Energy* 2017, **3**: 53–60.